The enhancement of Fermi-surface images in positron ACAR spectra

1995 J. Phys.: Condens. Matter 7 925

(http://iopscience.iop.org/0953-8984/7/5/015)

J. Phys.: Condens. Matter 7 (1995) 925–938. Printed in the UK

The enhancement of Fermi-surface images in positron ACAR spectra

K M O'Brien, M Z Brand, S Rayner and R N West
Department of Physics, University of Texas at Arlington, Arlington, TX 76019, USA

Received 26 August 1994, in final form 3 November 1994

Abstract. This paper describes a frequency-limited derivative technique that has dramatically increased our ability to resolve Fermi-surface discontinuities in our 2D ACAR spectra. The performance of the technique, which involves minimal CPU time, is demonstrated with example applications to both simulated and real 2D ACAR spectra.

1. Introduction

In the typical 2D ACAR apparatus [1], such as that in our own laboratory, low-energy positrons from a ^{22}Na source bombard a single-crystal sample held under vacuum in an appropriately constructed and shielded chamber. On entering the specimen, each positron rapidly thermalizes (in a time of the order of picoseconds) and eventually (in a time of the order of 100 ps) annihilates with one of the electrons in the sample. The relative directions of photon pairs resulting from the two-photon mode of annihilation are recorded on a pair of opposed and distant (typically 10–20 m) position-sensitive detectors operated in a coincidence mode. In the centre-of-mass frame of each such event the photons emerge with equal energies in exactly opposite directions. In the laboratory frame, the centre-of-mass momentum ($\langle p \rangle \sim 10^{-2} m_0 c$) is essentially that of the electron because the positron is thermal. The transverse (to the detector–sample–detector axis) components p_x, p_y of that centre-of-mass momentum produce small deviations from antiparallelism ($\theta = p_x/m_0c$, $\phi = p_y/m_0c$; $\langle\theta\rangle$, $\langle\phi\rangle \sim 10$ mrad (1 mrad = 0.14 au)) in the relative photo-emission directions. The remaining longitudinal component p_z causes an equal and opposite ($\pm cp_z/2$) small Doppler shift in the energy of each photon.

In 2D ACAR experiments the Doppler shifts are not resolved. Thus, the measured transverse-momentum spectra amount to 2D projections or integrals (along the major detector–sample–detector axis) of some 3D electron–positron momentum density [2]. In most measurements the samples are oriented such that the integration direction is a high-symmetry direction of the crystal. The data are mapped, with the aid of appropriate hardware and software, onto a discrete array of bins (typically $256 \times 256 \sim 0.15$ mrad^2 bins). The resulting spectra are initially corrected with a momentum sampling function, which eliminates effects arising from the finite size of the detectors and any non-uniformities in their response [1]. Then they are further processed and analysed according to the needs of the problem at hand.

Recent investigations of the electronic structure of complex systems, such as high-temperature superconductors and heavy-fermion systems, have led to the adoption of a number of new and relatively sophisticated 2D ACAR spectrum image-enhancement techniques. They have included linear and non-linear digital procedures for deconvolution

0953-8984/95/050925+14$19.50

of instrumental smearing effects, noise smoothing and data modelling [3, 4]. Our major preoccupation has been to isolate the contribution of the Fermi surface to the 2D ACAR spectra for various conductors. In this paper we will describe a simple digital operation that can isolate these Fermi-surface signals in a CPU time of only a few seconds.

2. 2D ACAR and its spectra

The 3D electron–positron momentum density, from which the integrated 2D ACAR spectra derive, is most easily described [2], in a one-electron approximation, as a sum of individual contributions from occupied states of energy-band index n and reduced Bloch wave vector k. These contributions occur at points $p = \hbar(k+G)$, where G is any reciprocal lattice vector, throughout the density with intensities that are determined by the electron and positron wave functions. The consequent overall contribution from each band has the full point symmetry of the crystal lattice and an overall shape that reflects the nature of the states in that band. For a full band it is continuous. For a part-full band there are, in addition, discontinuities at all points $p_F = \hbar(k_F + G)$. The loci of those discontinuities mark the Fermi surface. Wherever that surface lies normal to the plane of projection a corresponding pattern of discontinuities appear in the 2D spectrum.

A complete and detailed interpretation of a measured spectrum, in terms of the nature and form of the occupied states, is seldom possible without a complementary, detailed band-theoretical calculation that includes a non-trivial treatment of positron–ion and positron–electron interactions. Frequently, however, the determination of just the Fermi surface is sufficient to make the study worthwhile. Nevertheless, the identification of the distributed Fermi-surface discontinuities in a momentum density in the presence of other wave-function-related structures, instrumental smearing effects and statistical noise is not always easy. When it is not, as is often the case in studies of electronically complex multiband systems, an LCW transformation can be useful. In an LCW transformation the integrated momentum density is folded back into a primitive cell of the (projected) reciprocal lattice [5]. The LCW transformed density causes the Fermi-surface structures that were originally distributed throughout the momentum density to be brought together into a set of coherent and reinforced images of the Fermi surface in the equivalent region of k space. The continuous (full-band) parts of the original density sum into a high-intensity but relatively slowly varying background, which, because of the translational symmetry implied in the transformation, must have the form of a simple linear superposition of cosines [6]. Our own studies of various insulators and semiconductors have shown that this superposition is dominated by a few predominantly long-wavelength cosines. Therein lies the power of the derivative filter technique we will now describe.

3. The derivative filter technique

A measured momentum (or a derived LCW) density M is a statistically limited, instrumentally smeared, histogram representation of the ideal equivalent density N. That is,

$$M = R \otimes N(F + E) + S \tag{1}$$

where R is the inherent resolution function of the detection apparatus, F represents the Fermi-surface structures, E the remaining wave-function-related structures (in an LCW

density, the cosines) and S the statistical noise. The spectral weight of the resolution-smeared Fermi-surface structures extends (see below) from low frequencies to an effective high-frequency limit dictated by the strength of the singularities in N and the prevailing resolution. The contribution due to E is predominantly at low frequencies. The components of S that have the most deleterious effects on the images of F are those at the higher frequencies. Thus, a suppression of the lowest (mainly due to E) and highest (mainly due to S) frequencies in M should enhance the Fermi-surface images.

Digital data filters based on simple spatial-averaging techniques are often used to enhance 2D images [7]. Spatial averaging or smoothing suppresses noise and is equivalent to a low-pass filter. A high-pass filter can be effected by subtracting the output of a low-pass filter, involving a relatively broad smoothing function, from the original image. A band-pass filter can then be achieved by performing a final light (narrow-smoothing-function) smoothing of the high-pass filter result. This is the procedure we are now using on 2D ACAR images. In brief, we first perform

$$M_{\mathrm{h}} = M - w_{\mathrm{n}} \otimes M \tag{2}$$

with a simple, unweighted normalized $(n \times n)$-channel mask with n equal to or greater than the FWHM $r(\sim \sigma_r)$ of the 2D resolution function. That suppresses a large part of E. Then, when appropriate we perform

$$M_{\mathrm{bp}} = w_{\mathrm{m}} \otimes M_{\mathrm{h}} \tag{3}$$

another unweighted $m \times m$ mask $(m < r)$ to suppress the residual noise.

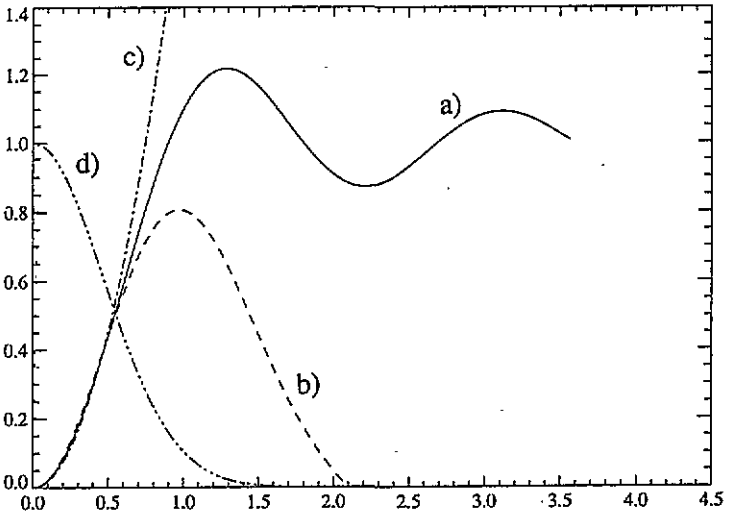

Figure 1. The spectral modulation functions for the various operations defined in the text: (a) a high-pass filter (with $n = 7$); (b) a band-pass filter (with $n = 7$, $m = 3$); (c) double differentiation; (d) instrumental smearing ($r = 5$).

The effect of these operations is most easily seen in the 'frequency' $q = 2\pi/\lambda$ domain wherein the various convolutions transform into simple products. In the continuous limit, the Fourier transform (FT) of an unweighted mask of width n (for simplicity we set the

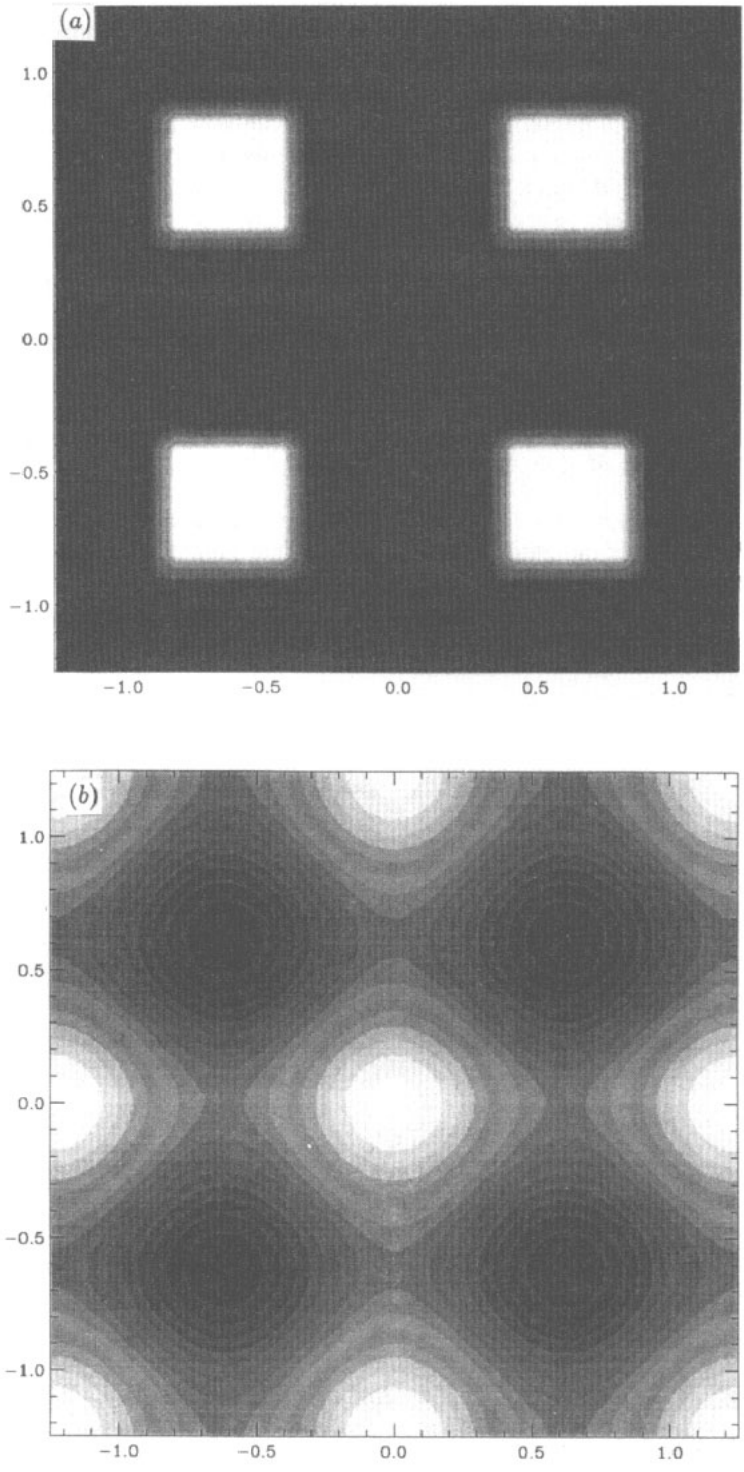

Figure 2.

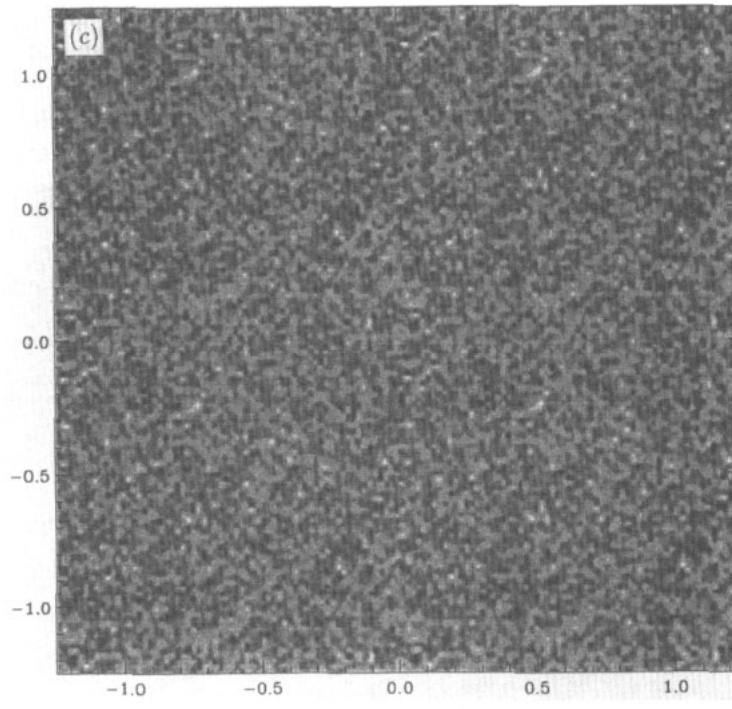

Figure 2. Images of the simulation components: (a) the 'Fermi surface'; (b) the background cosines; (c) the statistical noise.

channel width equal to one) is $\mathrm{sinc}(qn/2)$. Thus, the FT of M_h is the FT of M modulated by $\chi_{hp} = \{1 - \mathrm{sinc}(qn/2)\}$. χ_{hp} is the 'spectral modulation function' for the high-pass-filter operation. For the band-pass filter $\chi_{bp} = \{\mathrm{sinc}(qm/2)\}\{1 - \mathrm{sinc}(qn/2)\}$. The form of these functions is illustrated in figure 1. Their effect on the spectrum to which they are applied depends on its spectral density, but the spectral density of the significant information in our 2D ACAR spectra is confined by the (assumed Gaussian) experimental resolution FWHM r to a range of $q <\sim 5/r$. Over much of this range (figure 1) both χ functions are close to q^2 and the effect of them is roughly equivalent to double differentiation and multiplication by -1. The second derivatives of ACAR spectra have occasionally been used in the past [8] in Fermi-surface investigations but the amplification in high-frequency noise that always accompanies the differentiation of imperfectly defined numerical data has limited their usefulness. Here, at higher q, χ_{hp} saturates and the noise problem is much less, with or without the final stage of smoothing. Therein, and in the simplicity and speed of its implementation, lie the strength of this 'frequency-limited-derivative' (FLD) approach.

4. 2D simulations

In order to become better acquainted with the capabilities and the limitations of the FLD procedure we have applied it to simulated 2D LCW densities with data and measurement parameters similar to those obtained in our work of the last few years on high-temperature cuprate superconductors. Each simulation, on a square array of side $L = 64$ channels, involved (figure 2) three contributions: a 'Fermi surface' comprising a central square

region of height ΔN_F, convoluted with a Gaussian resolution function of FWHM five channels; a background $N(E) = N_0\{1 + 10^{-2}[\cos(2\pi p_x/L) + \cos(2\pi p_y/L)]\}$ with an overall dynamic range $\Delta N_E = 4 \times 10^{-2} N_0$; and additive noise of standard deviation $\sigma = \Delta N_S \approx (N_0)^{1/2} (\approx (\bar{N})^{1/2})$. In the processing (equations (2) and (3)), n was set to five and m to three.

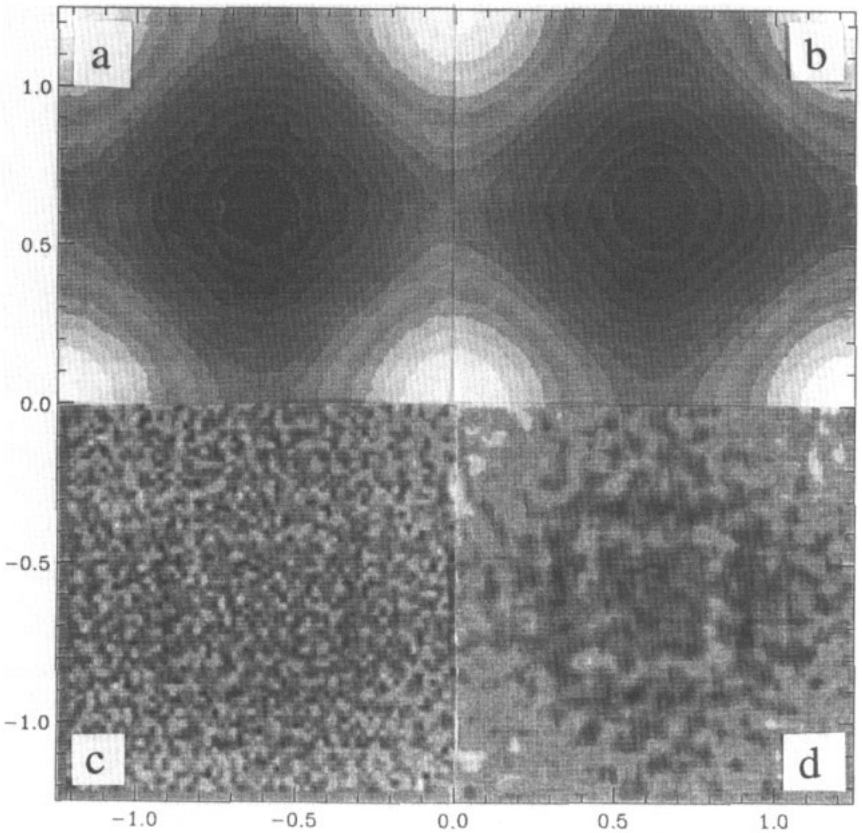

Figure 3. A simulation with $\Delta N_E = 10\Delta N_F$ and $\Delta N_F = 5\sigma$: (a) before processing; (b) (a) after smoothing with a (5 × 5)-channel unweighted mask; (c) (a) minus (b); (d) (c) after smoothing with a (3 × 3)-channel mask.

In figures 3–5 we show the effect of the various steps on three simulated spectra with $\Delta N_E = 10\Delta N_F$ and different levels of noise (σ). In the raw spectra, shown in the upper left quarter of each figure, the effect of the dominant cosine background in obscuring the Fermi-surface images is obvious. The reappearance of the Fermi-surface images, or more properly, something close to the negative of their second derivatives, in the third and fourth quarters is equally clear. With these particular choices of signal and cosine background the minimal conditions for visual identification of the signal images are $\Delta N_E \leqslant 25\Delta N_F$ and $\Delta N_F \geqslant 3\sigma$ but more stringent conditions would undoubtedly apply for the resolution of the weaker discontinuities arising from Fermi surfaces of a more complex geometric form. If $\Delta N_E \leqslant 20\Delta N_F$ and $\Delta N_F \geqslant 5\sigma$, a search for the most prominent 'zero crossings' in individual rows and columns of the filtered arrays allows the positions of the Fermi-surface breaks to be established to within one-half of a channel. This is remarkable when one

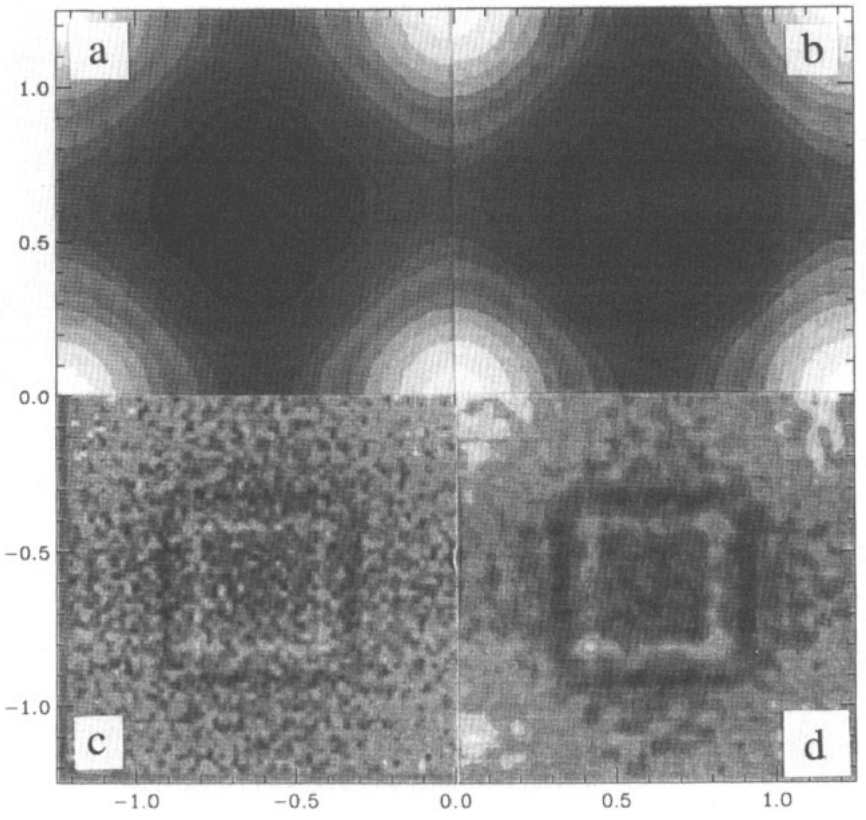

Figure 4. A simulation with $\Delta N_E = 10\Delta N_F$ and $\Delta N_F = 10\sigma$. The presentation is as for figure 3.

recalls that the resolution FWHM $r = 5$ channels. It must be added that the process creates artifacts in the neighbourhood of the original discontinuities. Note that throughout the final spectra the centres of the squares are no longer flat. This generic effect of the processing must always be taken into consideration when the FLD spectra are interpreted. When the process is applied to an array with $\Delta N_E = 0$ it is, not surprisingly, a hindrance rather than a help.

The values of parameters used in these simulations (i.e. mask widths, cosine amplitudes, resolution, etc) reflect, in the main, those we have used and/or that have applied to much of our recent experimental data. We have chosen throughout to smooth with unweighted masks. We have tried other functions (for example Gaussians) but have always obtained essentially identical results. There is an equally marked insensitivity in respect to the width of the first smoothing function. Here we have used a (5×5)-channel mask primarily to limit array edge effects. In our analyses of real data, we have often used this same mask, but other choices of mask width, even as large as 25×25 channels, yield virtually identical derivative spectra.

5. Real applications

We have applied the FLD technique to many different sets of experimental 2D ACAR data

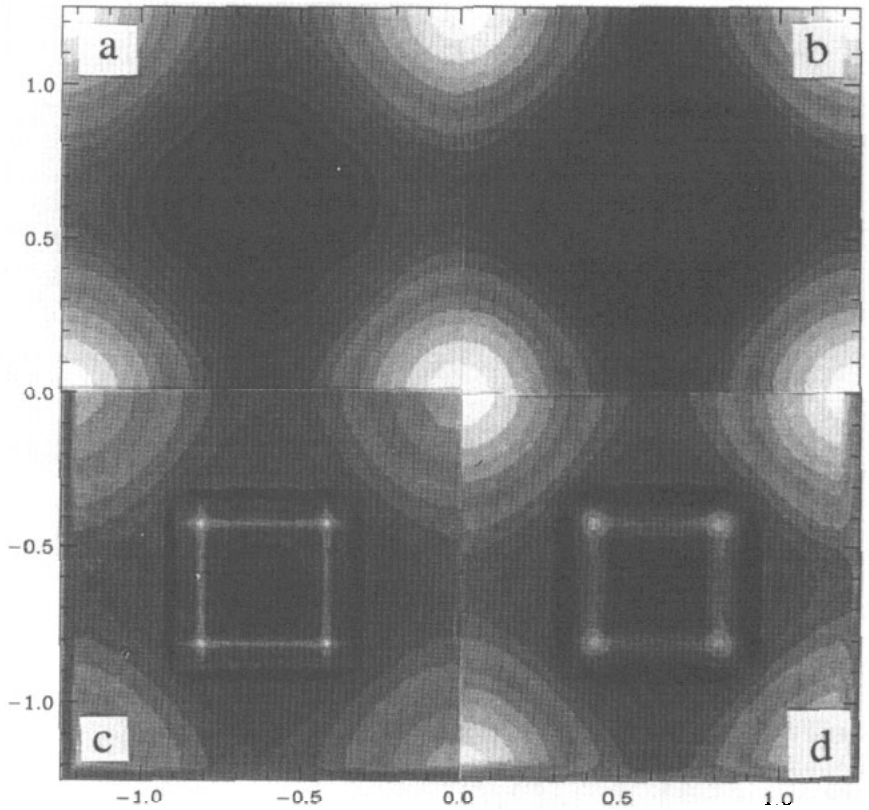

Figure 5. A simulation with $\Delta N_E = 10\Delta N_F$ and $\sigma = 0$. The presentation is as for figure 3.

with almost universally good results. In the interests of space we shall present only a few of our spectra here.

The LCW transformation is seldom applied to the 2D ACAR results for metals with relatively simple s–p conduction bands because (i) the Fermi-surface images are usually already clear in the original momentum spectra and (ii) it can sometimes give misleading results. Cu is a case in point. When the integration direction (see section 1) is [111] an LCW transformation provides a remarkable picture of the Cu Fermi surface in the repeated-zone scheme [9] but, when the integration direction is [100], the Fermi-surface signals are completely obscured by large-amplitude cosines (figure 6(a)). The removal of those cosines and the remarkable exposure of a Fermi-surface image in good agreement with theory is evident in figure 6(b) and (c). These observations apply equally well to the [100] LCW spectra for other noble metals and alloys.

LCW spectra for the BCC transition metals usually provide a good image of the multisheet Fermi surfaces of these systems without FLD processing but, we have found, generally benefit from it. In some instances the effect of the process is startling. Figure 7 shows its effect upon the [0001] projected LCW spectrum for Y. Our theoretical calculations (unpublished) of the occupation density expose a great deal of detail concerning the Fermi-surface topography. We note, for example, the small maxima around M and the sixfold 'rosette' contours encircling Γ. These features are barely discernible in the raw LCW data but in the derivative they are perfectly clear. The small maximum around Γ in the filtered array is the artifact

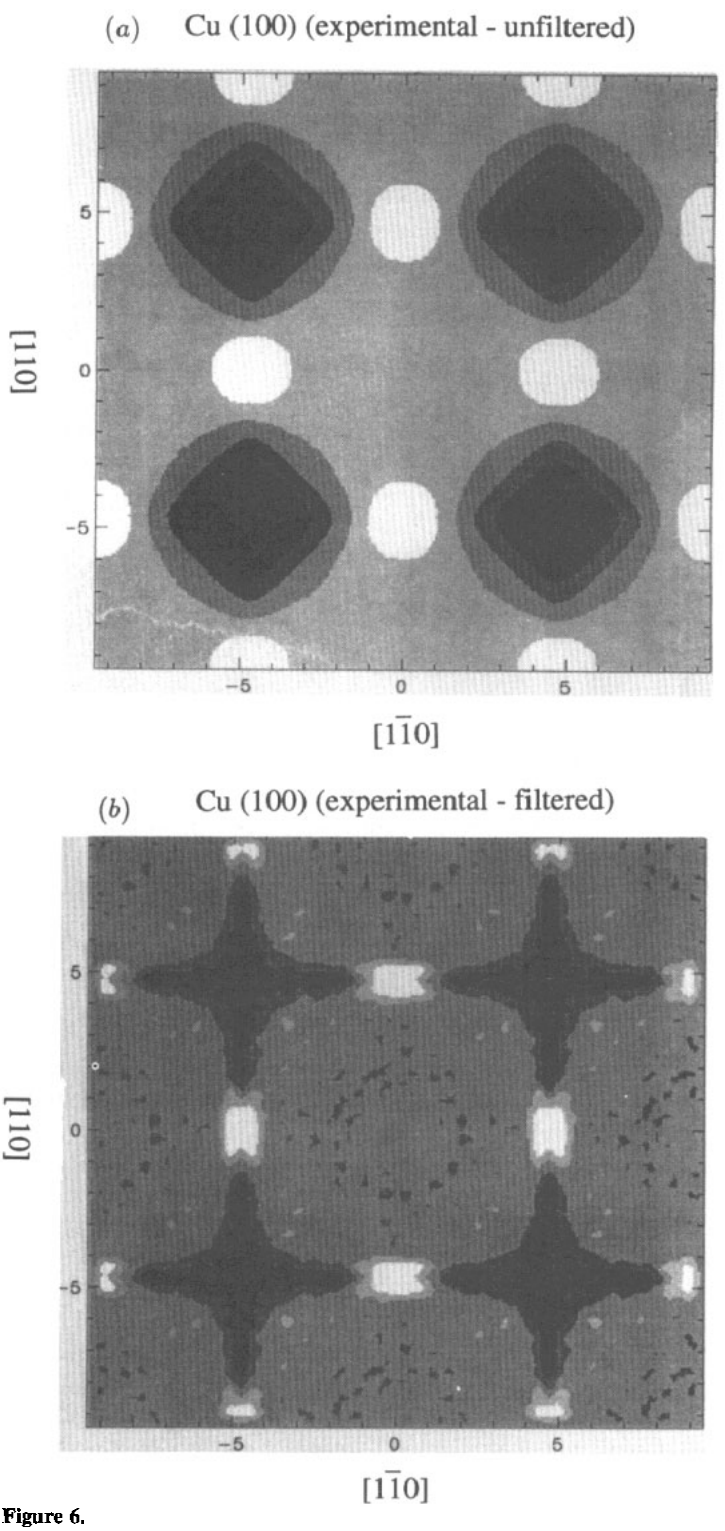
(a) Cu (100) (experimental - unfiltered)
5
0
-5
[110]
-5
0
5
[1$\bar{1}$0]
(b) Cu (100) (experimental - filtered)
5
0
-5
[110]
-5
0
5
[1$\bar{1}$0]

Figure 6.

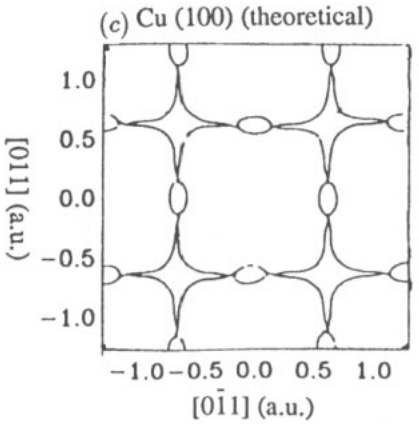

Figure 6. LCW densities for Cu, [100] integration: (a) symmetry-folded 'raw' data; (b) FLD data; (c) the Cu Fermi surface according to Halse [14].

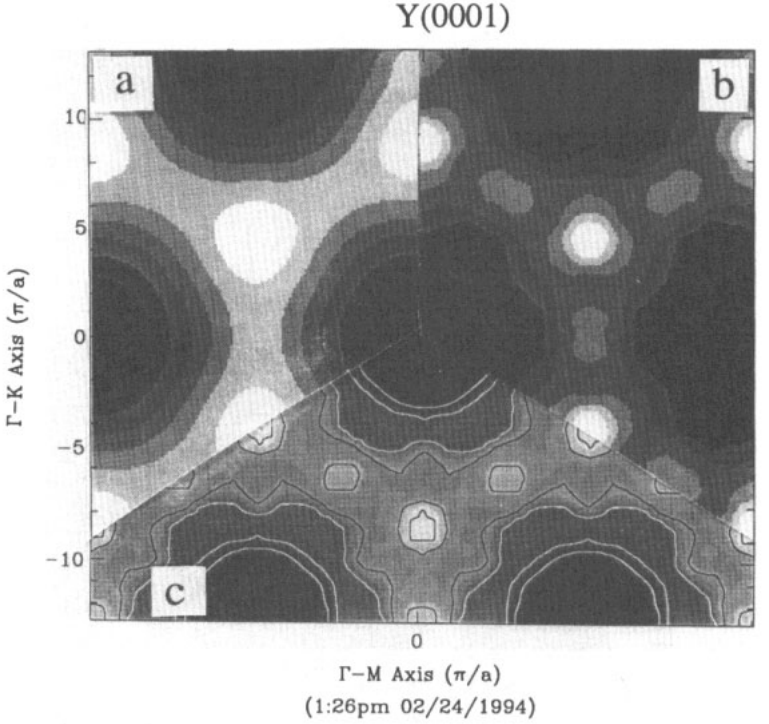

Figure 7. LCW densities for Y, [0001] integration: (a) symmetry-folded data; (b) filtered experimental data; (c) the theoretical density.

discussed in section 4.

One of the most difficult questions the 2D ACAR technique has been asked to address is that concerning the existence of Fermi surfaces in the ceramic high-temperature superconductors. It was this problem that led us to the present work. In the earliest successful studies [10, 11] of $YBa_2Cu_3O_{7-\delta}$ (YBCO), the existence of a major 'ridge' (along Γ-X) Fermi-surface section, predicted by theory and associated with states on Cu–O chains, was clear from structures seen in both the measured 2D momentum and the corresponding

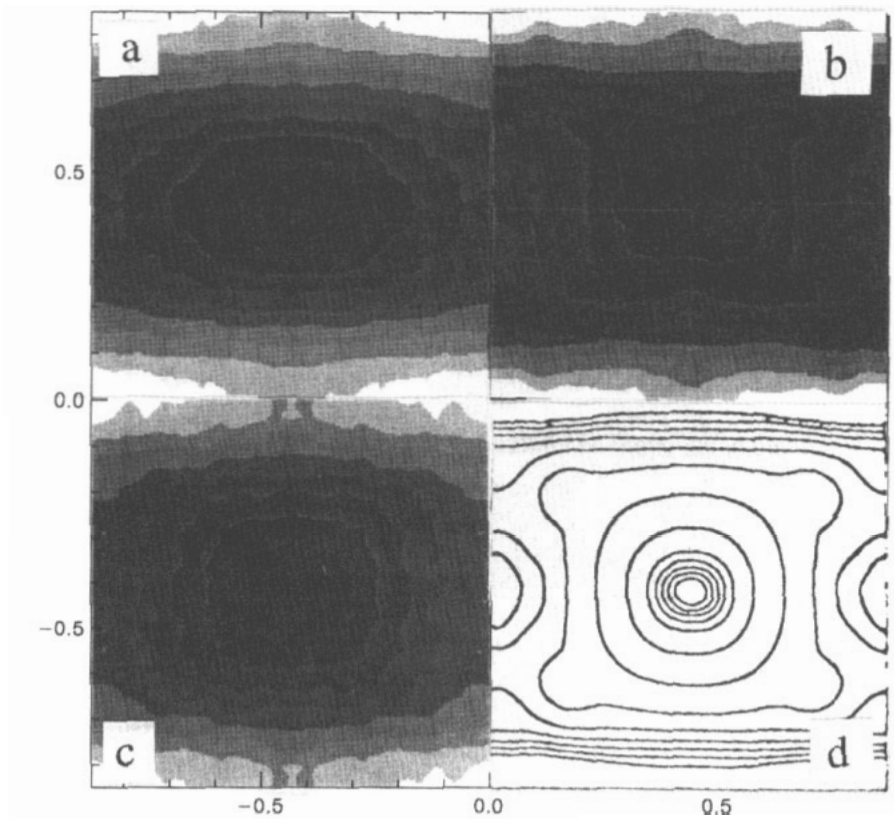

Figure 8. LCW densities for $YBa_2Cu_3O_{7-d}$ (YBCO), [001] integration: (a) symmetry-folded data; (b) FLD data; (c) cosine-corrected data; (d) the theory according to Berko *et al* [12].

LCW spectra. Evidence for other Fermi-surface sections associated with the Cu–O planes was less easy to argue. The theories [12] predicted additional weaker close-to-square hole sections centred on S. Figure 8 shows the relevant (integration direction along [001]) LCW spectra. In the unprocessed spectrum (a) the contours encircling the S point are elliptic rather than square. In an earlier paper [10] we described how a single 'cosine correction', based on symmetry considerations, could make those contours more square (c). In the derivative spectrum (b) the geometric forms predicted by the theory (d) are again perfectly clear. In such complex multiband systems the FLD procedure can prove invaluable. It has been recently applied to data for the heavy-fermion system CeB_6 and there [13], again, has disclosed a Fermi surface in good accord with theory and DHVA results.

Thus far, all our discussions and our examples have concerned situations where the FLD process is applied to the folded LCW spectra, but one can equally well apply the process to 2D ACAR momentum spectra prior to LCW folding and, after folding, obtain essentially the same final result. Figure 9 compares unprocessed (but corrected and symmetrized) and processed momentum densities for Nb together with the theoretical 2D $\boldsymbol{k}$-space occupation density [13]. Even at this stage the essential topography of the Fermi surface is clear. The corresponding LCW spectrum is also in much better agreement with the predictions of the band-structure theory than its unprocessed counterpart.

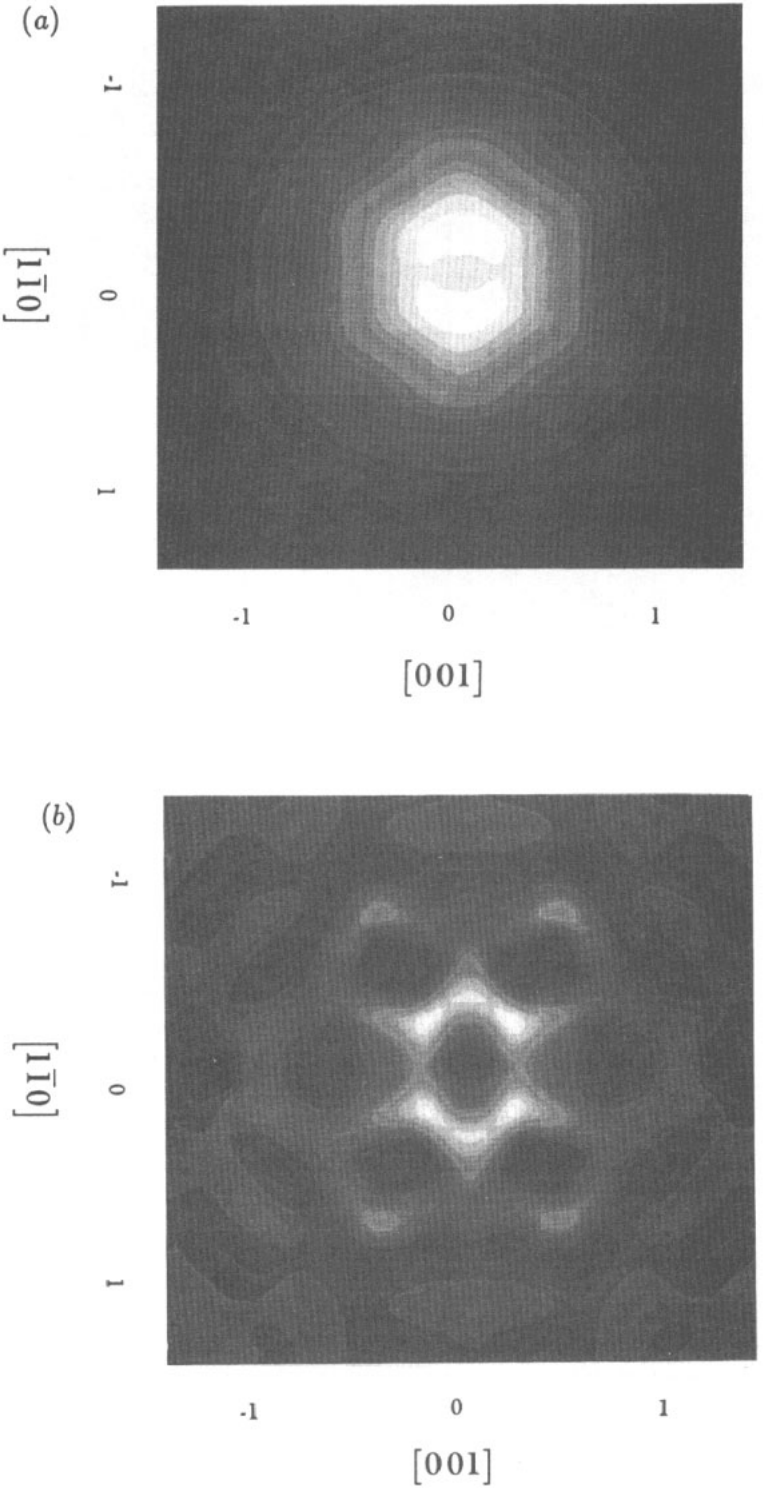

Figure 9.

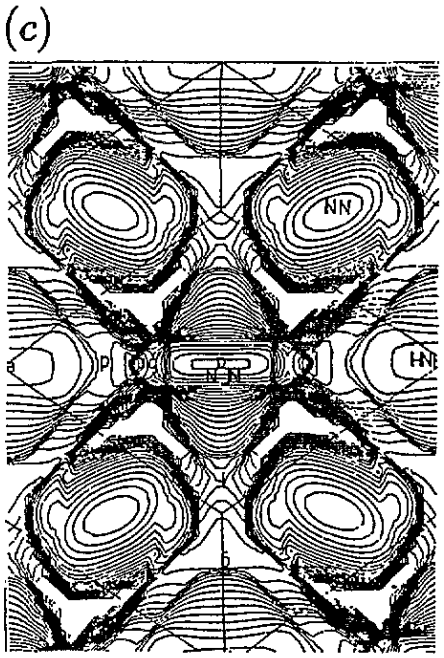

Figure 9. 2D momentum densities for Nb, [110] integration: (a) symmetry-folded data; (b) FLD data; (c) the theoretical prediction by Kaiser *et al* [8].

6. Conclusions

We have described a rapidly executable frequency-limited derivative technique, which, when applied to 2D ACAR data, enables Fermi surfaces to be resolved in the presence of large-amplitude error signals and considerable amounts of statistical noise. Simulations have shown that a Fermi surface can be resolved in an LCW spectrum if the Fermi surface breaks are greater than or equal to three times the variance of the statistical noise present, even when they are masked by error cosines of much greater amplitude. Applications of this filter on experimentally obtained 2D ACAR spectra invariably improves the agreement between experiment and the predictions of band-structure theory.

Acknowledgments

The authors would like to thank the Texas Advanced Research Program and the Robert A Welch Foundation for providing the grants that have made this work possible.

References

[1] West R N, Mayers J and Walters P A 1981 *J. Phys. E: Sci. Instrum.* **14** 478
[2] Berko S 1983 *Positron Solid-State Physics* ed W Brandt and A Dupasquier (Amsterdam: North-Holland) p 64
[3] Hoffmann L, Shukla A, Peter M, Barbiellini B and Manuel A A 1993 *Nucl. Instrum. Methods* A **335** 276

[4] Manuel A A 1993 *Positron Spectroscopy of Solids (Proc. Int. School Phys. 'Enrico Fermi' Course CXXV)* ed A Dupasquier at press
[5] Lock D G, Crisp V H C and West R N 1973 *J. Phys. F: Met. Phys.* **3** 561
[6] Lock D G and West R N 1975 *Appl. Phys.* **6** 249
[7] Jain A K 1989 *Fundamentals of Digital Image Processing* (Englewood Cliffs, NJ: Prentice-Hall)
[8] Kaiser J H, Walters P A, Bull C R, Alam A, West R N and Shiotani N 1987 *J. Phys. F: Met. Phys.* **17** 1243
[9] West R N 1980 *Physics of Transition Metals 1980 (Inst. Phys. Conf. Ser. 55)* ed P Rhodes (Bristol: Institute of Physics) ch 1, p 35
[10] Haghighi H, Kaiser J H, Rayner S, West R N, Liu J Z, Shelton R, Howell R H, Solal F and Fluss M J 1991 *Phys. Rev. Lett.* **67** 382
[11] Smedskjaer L C, Bansil A, Welp U, Fang Y and Bailey K G 1991 *J. Phys. Chem. Solids* **52** 1541
[12] Berko S, Singh D J and von Stetten E C 1991 *J. Phys. Chem. Solids* **52** 1485
[13] Biasini M, Alam A M, Harima H, Onukid Y, Fretwell H and West R N 1994 *J. Phys.: Condens. Matter* **6** 7823
[14] Halse M R 1969 *Phil. Trans. R. Soc.* **265** 507